Supplement of Atmos. Chem. Phys., 20, 13283–13301, 2020
https://doi.org/10.5194/acp-20-13283-2020-supplement

Atmospheric Chemistry and Physics
Open Access
EGU

Supplement of

Impact of biomass burning aerosols on radiation, clouds, and precipitation over the Amazon: relative importance of aerosol–cloud and aerosol–radiation interactions

Lixia Liu et al.

Correspondence to: Yafang Cheng (yafang.cheng@mpic.de) and Hang Su (h.su@mpic.de)

Contents of this file

Introduction

Text S1 includes the observation data used in the model evaluation. Text S2, Table S2 and Figures S2–S6 include the model evaluation of the meteorological conditions. Text S3, Table S3 and Figures S7–S9 include the model evaluation of the aerosol field. Descriptions of Tables S1, Table S4, Figures S1 and Figures S10–S14 are shown in the corresponding caption.

Text S1

Observation data

1 Ground based measurements at ATTO

The Amazon Tall Tower Observatory (ATTO) site is located in the central Amazon, about 150 km northeast of Manaus, Brazil (Fig. 1), and represents a relatively clean rainforest background environment (Andreae et al., 2015). An 80-m tower, embedded within the canopy of about 35 m height, provides continuous measurements related to the research fields of meteorology, atmospheric trace gases, and aerosols (Andreae et al., 2015). Observational datasets used in this paper include meteorological variables, cloud condensation nuclei (CCN) number concentrations, and black carbon (BC) mass. Meteorology observations were obtained from a thermohygrometer and a 2-D sonic anemometer installed at 55 m on the tower. The data was averaged at 10-min resolution from raw observations taken at 1-min resolution. Air temperature and relative humidity (RH) measurements are only available from 1 Sep to 23 Sep 2014, while wind speed was observed over the complete simulation period. Aerosols were sampled at 60 m height. The CCN number concentration measurements by a CCN counter with supersaturation cycling through a set of levels ranging from 0.11% to 1.1% were used in this study. Detailed information on the CCN dataset can be found in Pöhlker et al. (Pöhlker et al., 2016, 2018). Equivalent black carbon (BCe) mass concentrations, M_{BCe}, were obtained from a multi-angle absorption photometer (MAAP; μg m^{-3}). The mass concentration was calculated by dividing the absorption coefficients at 637 nm by the dry season mass absorption cross section of 12.3 m^2 g^{-1} according to Saturno et al. (2018a). Specific details about the MAAP measurements of M_{BCe} can be found in Saturno et al. (2018a).

2 Radiosonde measurements

Radiosonde observations from the Integrated Global Radiosonde Archive (IGRA; Durre et al., 2006) at the site Manaus (3.15 °S, 59.98 °W) were used to evaluate the vertical profile of meteorological elements. The IGRA sounding observations were conducted at 00:00 and 12:00 Universal Standard Time (UTC, which is 4 hours before local time). Note that throughout this paper the time referred to is UTC, unless Local Time (LT) is specifically mentioned. Radiosonde measurements at standard pressure levels within the troposphere (100, 150, 200, 250, 300, 400, 500, 700, 850, and 1000 hPa), as well as derived characteristic indices for convection, e.g., Convective Available Potential Energy (CAPE) and Lifting Condensation Level (LCL), were compared with simulation outputs.

3 TRMM

The Tropical Rainfall Measuring Mission (TRMM) 3B42 (Huffman et al., 2007) product was employed to evaluate the precipitation simulation performance. TRMM provides satellite observations of tropical and subtropical (50 °S–50 °N) precipitation globally. The 3B42 rainfall dataset produces 3-hour averaged high-quality infrared and microwave precipitation estimates at a resolution of 0.25° × 0.25° (Huffman et al., 2007).

4 MODIS

The Moderate Resolution Imaging Spectroradiometer (MODIS) Level 3 products provide satellite-derived daily estimates of cloud properties at a resolution of 1° × 1° (Platnick, S., et al., 2015). The measurements by MODIS onboard Aqua were used in this study, as the passing time of Aqua is approximately at 13:30 LT, when the local convective system is highly developed (Koren et al., 2004). The retrieval of cloud fraction, total liquid water path (LWP), and total ice water path (IWP) were compared with the corresponding modeling results. Model outputs at the satellite detection time were used when comparing against MODIS data.

5 AERONET

The Aerosol Robotic Network (AERONET) is an observation network of about 100 sites distributed globally, providing continuous measurements of aerosol optical properties (Holben et al., 2001). The observations are made by sun- and sky-scanning ground-based automated radiometers at various wavelengths. The aerosol optical depth (AOD) at 550 nm was interpolated using corresponding measurements at 675 nm and 440 nm. The level 2.0 cloud-screened product was used in this study. The observation data was retrieved for the site Manaus_EMBRAPA (2.89 °S, 59.97 °W) over September 2014.

6 CALIPSO

The Cloud-Aerosol Lidar and Infrared Pathfinder Satellite Observations (CALIPSO) Level 3 aerosol product (Tackett et al., 2018) is a global gridded dataset with a horizontal resolution of 2° × 5°, which provides monthly mean layered aerosol optical properties with a vertical resolution of 60 m for the troposphere below 12 km. The clear-sky retrieval of aerosol extinction at 532 nm was used to evaluate the vertical profile of the simulated aerosol. Both daytime and nighttime measurements over the studied region were utilized to provide the general vertical characteristics of aerosols.

Text S2

Evaluation of meteorological condition

Figure S2 shows the time series of hourly surface meteorological variables observed at the ATTO site and corresponding simulated results from domain3 in September 2014. As the canopy effect is integrated in the land surface model (Lee et al., 2016), the simulated meteorological variables are characterized by above-canopy properties. The variation patterns of the air temperature and RH are well captured by the model, with correlation coefficients of 0.86 and 0.78, respectively (Table S2). The surface air temperature is reproduced with a moderate overestimation of 0.2 °C (Table S2), which mainly occurs on 6 Sep, 8 Sep, and 17–18 Sep, whereas the RH exhibits an opposite bias. These significant biases occur corresponding to the missing prediction of rainfall on 6 and 18 Sep and underprediction of precipitation on 8 and 17 Sep by the model at this site (Fig. S3). This is expected since precipitation enhances surface evaporation and latent heat flux, leaves less net energy in the ground to heat the surface air (Zhuang et al., 2017), and therefore corresponds to a cool and moistened near-surface atmospheric state as can be found in the ATTO observation (Fig. S2). Consequently, the precipitation underestimation in the model was accompanied by higher biased simulated temperature and lower biased RH. This discrepancy between simulated and observed precipitation at the ATTO site could be associated with a bias of rainfall location and existence of unresolved subgrid-scale (<3 km) precipitation, which will be further discussed later by comparing with the regional rainfall prediction. The wind speed from the simulation is generally lower than the observations with an average bias of –0.2 m s^{-1} (Table S2). The underestimation of the surface wind speed by the model also existed extensively in previous WRF-Chem simulations, and was ascribed to uncertainties in surface drag parameterization (Tuccella et al., 2012; Zhang et al., 2015).

The vertical distribution of the meteorological variables at the Manaus site over the 30-day simulation period is compared in Fig. S4. To keep consistency, simulation outputs of temperature and RH from domain3 were interpolated to the standard levels of the radiosonde data. The CAPE and LCL, inferred from the temperature and humidity profiles from the simulation and observation, are also shown. The model reproduces the air temperature profiles well. The RH generally follows the observed results below 300 hPa, while in the upper troposphere above 300 hPa a large overestimation occurs at 12:00 UTC.

Similarly, an overestimation of simulated water vapor compared with MLS retrievals in the upper troposphere was found in WRF-Chem simulations of the Amazon Basin (Wu et al., 2011). The CAPE and LCL values estimated from the model agree well with that from the observations at 00:00 UTC. Noticeable differences of CAPE and LCL between model and observation of 240 J kg^{-1} and –266 m, respectively, are seen at 12:00 UTC, implying a possible earlier development of the simulated planetary boundary layer (PBL) ahead of observations.

The daily retrievals of cloud fraction, total LWP, and total IWP from the MODIS Aqua measurements are used to evaluate the simulation performance for cloud properties by WRF-Chem. The domain3 simulation results are averaged over the domain area to compare with the corresponding variables from the satellite measurements, as shown in Fig. S5. The simulated total LWP, calculated as the sum of liquid cloud and rainwater, correlates well with observations with a moderate underestimation. The total IWP from the model, as the sum of cloud ice, snow, and graupel, basically shows a positive correlation with the observations. However, a large underestimation of the total IWP from the model exists compared to the remote-sensed data. The model performs relatively well for the extreme low and high IWP regimes, with values being approximately 25% of the observations. The simulation of the total IWP by the WRF model has been found to produce a seasonally averaged underestimation by up to 80% compared with satellite measurements (Baro et al., 2018). The uncertainties inherent in the satellite dataset, e.g., eliminating data points with unrecognized cloud ice, would bias the observation results towards higher values and thus to some extent account for the discrepancy between model and observation. Besides, uncertainties associated with the ice-phase microphysical processes, e.g., the lack of IN parameterization, may also be a potential reason for this discrepancy (Su et al., 2018). Generally, the total cloud fraction from the model shows a linear correlation with the observations, falling between 25%–75% of the observed values.

Figure S6 shows the time series of domain-averaged 3-hour accumulated precipitation from the domain3 simulation and corresponding TRMM measurements during September 2014. The model well captures the occurrence of rainfall measured remotely by satellite. The regional rainfall events on 6, 8, 17, and 18 Sep are well predicted by the model with a slight underestimation, which reflects a better model performance compared with the evident model underestimation of precipitation at the ATTO site on these four days. Moreover, the modeled synoptic patterns corresponding to the precipitation episodes are consistent with the NCEP reanalysis data (not shown). The well-reproduced regional synoptic and precipitation conditions in the model serve to corroborate that the precipitation underestimation at the ATTO site is likely induced by a local bias of rainfall location and neglecting precipitation from subgrid convection by the model. Generally, the simulated precipitation is comparable with TRMM observations in terms of time variation and intensity, which illustrates the model's ability to represent the convective activity during the study period.

Test S3

Evaluation of aerosol field

Table S3 shows the comparison of the modeled AOD against the AERONET observation at Manaus_EMBRAPA, a forest reservation site representative of the central Amazon environment (Artaxo et al., 2013). The model simulation generally captures the absolute value and the temporal variation of the observed AOD, with the mean bias and correlation coefficient being -0.03 and 0.54, respectively (Table S3). This is basically consistent with the AOD prediction accuracy in the Amazon by global models using the same fire emission inventory (Reddington et al., 2019; Pan et al., 2020). The slightly low bias in the AOD value could be related to an underestimated BB emission intensity due to errors in the detection of fires by satellite (Rosario et al., 2013) and/or an underestimation of the transatlantic transport from Africa (Holanda et al., 2020). Besides, the lack of SOA production in the model may also account for the bias in the AOD simulation (Bond and Bergstrom, 2006).

The simulated single scattering albedo (SSA) is compared with observations from previous studies, as shown in Table S3. Compared with the in-situ measured SSA of 0.87±0.06 at 637 nm at the TT34 tower (Rizzo et al., 2013) in the central Amazon, a slightly higher value of 0.89±0.01 is obtained by the model simulation. Similarly, the modeled monthly mean SSA of 0.90 for the location of the ATTO site is relatively higher than an extrapolated value of 0.88 at 550 nm from multi-year observations for the dry season at the ATTO site (Saturno et al., 2018b). Given the substantial influence of BB particles on the aerosol SSA (Saturno et al., 2018b), the difference between model results and observation may be associated with the mismatched average time periods for the comparison. Generally, the simulated SSA does not deviate greatly from the observed value, which reflects a reasonable representation of the aerosol optical characteristics in the model. In Fig. S7 we compare the time variation of black carbon mass concentration measured at the ATTO site during the simulation period with the simulation outputs. The model results are in fair agreement with the observed BC concentrations, indicating a reasonable estimate of the influence from BB on this region.

The aerosol vertical distribution is evaluated using the CALIPSO-measured monthly mean clear-sky aerosol extinction profile averaged over the domain3 (Fig. S8). The simulation data was processed to align with the observation by using outputs corresponding to the passing time of the satellite, excluding cloudy grids with a cloud criterion of 1 g kg^{-1} and interpolating the extinction coefficient at 550 nm to 532 nm. The model reproduced the observed high aerosol extinction coefficient below 3 km and accurately captured the location of the two peaks at the surface and near 2 km respectively. Compared with the observation, the model overestimates the aerosol extinction above 3 km, which was also found in Wu et al. (2011). This discrepancy may be associated with an overestimated exchange between PBL and the free atmosphere by turbulent mixing and convective transport, an underestimation of precipitation scavenging, and/or an overestimated plume rise at some fire spots. Generally, the model reasonably simulated the aerosol vertical distribution, illustrating an acceptable performance of the plume rise parameterization. The ability of the model to reproduce the aerosol vertical pattern provides reliable aerosol

input for investigating the aerosol-radiation-cloud interaction, given the important role of the vertical distribution of light-absorbing aerosols in affecting the aerosol radiative effect (Johnson et al., 2004).

A comparison of CCN concentrations at different supersaturations between in-situ observation and the WRF-Chem simulation for the ATTO site is presented in Fig. S9. The calculation of CCN number concentration at observed supersaturation level from model outputs followed the method in Su et al. (2010). The model results show an overall agreement in magnitude with observations for the supersaturation range of 0.2-0.5%, which represents the typical atmospheric conditions during the dry season in the Amazon (Archer-Nicholls et al., 2016). The variation of CCN number with supersaturation level matches the pattern obtained by observation (Pöhlker et al., 2018), indicating a reasonable sensitivity of aerosol activation ability to varying supersaturation situations.

References

Artaxo, P., Rizzo, L. V., Brito, J. F., Barbosa, H. M. J., Arana, A., Sena, E. T., Cirino, G. G., Bastos, W., Martin, S. T., and Andreae, M. O.: Atmospheric aerosols in Amazonia and land use change: from natural biogenic to biomass burning conditions, Faraday Discuss., 165, 203–235, doi:10.1039/c3fd00052d, 2013.

Baro, R., Jimenez-Guerrero, P., Stengel, M., Brunner, D., Curci, G., Forkel, R., Nea, L., Palacios-Pena, L., Savage, N., Schaap, M., Tuccella, P., van der Gon, H. D., and Galmarini, S.: Evaluating cloud properties in an ensemble of regional online coupled models against satellite observations, Atmos. Chem. Phys., 18, 15183–15199, doi:10.5194/acp-18-15183-2018, 2018.

Durre, I., Vose, R. S., and Wuertz, D. B.: Overview of the Integrated Global Radiosonde Archive, J. Climate, 19, 53–68, doi:10.1175/Jcli3594.1, 2006.

Huffman, G. J., Adler, R. F., Bolvin, D. T., Gu, G. J., Nelkin, E. J., Bowman, K. P., Hong, Y., Stocker, E. F., and Wolff, D. B.: The TRMM multisatellite precipitation analysis (TMPA): Quasi-global, multiyear, combined-sensor precipitation estimates at fine scales, J. Hydrometeorol., 8, 38–55, doi:10.1175/Jhm560.1, 2007.

Holben, B. N., Tanré, D., Smirnov, A., Eck, T. F., Slutsker, I., Abuhassan, N., Newcomb, W. W., Schafer, J. S., Chatenet, B., Lavenu, F., Kaufman, Y. J., Castle, J. V., Setzer, A., Markham, B., Clark, D., Frouin, R., Halthore, R., Karneli, A., O'Neill, N. T., Pietras, C., Pinker, R. T., Voss, K., and Zibordi, G.: An emerging ground-based aerosol climatology: Aerosol optical depth from AERONET, J. Geophys. Res.-Atmos., 106, 12067–12097, doi:10.1029/2001jd900014, 2001.

Lee, C. B., Kim, J. C., Belorid, M., and Zhao, P.: Performance Evaluation of Four Different Land Surface Models in WRF, Asian J. Atmos. Enviro., 10, 42–50, doi:10.5572/ajae.2016.10.1.042, 2016.

Pan, X. H., Ichoku, C., Chin, M., Bian, H. S., Darmenov, A., Colarco, P., Ellison, L., Kucsera, T., da Silva, A., Wang, J., Oda, T., and Cui, G.: Six global biomass burning emission datasets: intercomparison and application in one global aerosol model, Atmos Chem Phys, 20, 969–994, doi:10.5194/acp-20-969-2020, 2020.

Platnick, S., et al.: MODIS Atmosphere L3 Monthly Product. NASA MODIS Adaptive Processing System, Goddard Space Flight Center, USA: http://dx.doi.org/10.5067/MODIS/MOD08_M3.006, 2015.

Pöhlker, M. L., Ditas, F., Saturno, J., Klimach, T., de Angelis, I. H., Araujo, A. C., Brito, J., Carbone, S., Cheng, Y. F., Chi, X. G., Ditz, R., Gunthe, S. S., Holanda, B. A., Kandler, K., Kesselmeier, J., Konemann, T., Kruger, O. O., Lavric, J. V., Martin, S. T., Mikhailov, E., Moran-Zuloaga, D., Rizzo, L. V., Rose, D., Su, H., Thalman, R., Walter, D., Wang, J., Wolff, S., Barbosa, H. M. J., Artaxo, P., Andreae, M. O., Pöschl, U., and Pöhlker, C.: Long-term observations of cloud condensation nuclei over the Amazon rain forest - Part 2: Variability and characteristics of biomass burning, long-range transport, and pristine rain forest aerosols, Atmos. Chem. Phys., 18, 10289–10331, doi:10.5194/acp-18-10289-2018, 2018.

Reddington, C. L., Morgan, W. T., Darbyshire, E., Brito, J., Coe, H., Artaxo, P., Scott, C. E., Marsham, J., and Spracklen, D. V.: Biomass burning aerosol over the Amazon: analysis of aircraft, surface and satellite observations using a global aerosol model, Atmos. Chem. Phys., 19, 9125–9152, doi:10.5194/acp-19-9125-2019, 2019.

Reid, J. S., Koppmann, R., Eck, T. F., and Eleuterio, D. P.: A review of biomass burning emissions part II: intensive physical properties of biomass burning particles, Atmos. Chem. Phys., 5, 799–825, doi:10.5194/acp-5-799-2005, 2005.

Rizzo, L. V., Artaxo, P., Muller, T., Wiedensohler, A., Paixao, M., Cirino, G. G., Arana, A., Swietlicki, E., Roldin, P., Fors, E. O., Wiedemann, K. T., Leal, L. S. M., and Kulmala, M.: Long term measurements of aerosol optical properties at a primary forest site in Amazonia, Atmos. Chem. Phys., 13, 2391–2413, doi:10.5194/acp-13-2391-2013, 2013.

Rosario, N. E., Longo, K. M., Freitas, S. R., Yamasoe, M. A., and Fonseca, R. M.: Modeling the South American regional smoke plume: aerosol optical depth variability and surface shortwave flux perturbation, Atmos. Chem. Phys., 13, 2923–2938, doi:10.5194/acp-13-2923-2013, 2013.

Saturno, J., Ditas, F., Penning de Vries, M., Holanda, B. A., Pöhlker, M. L., Carbone, S., Walter, D., Bobrowski, N., Brito, J., Chi, X., Gutmann, A., Hrabe de Angelis, I., Machado, L. A. T., Moran-Zuloaga, D., Rüdiger, J., Schneider, J., Schulz, C., Wang, Q., Wendisch, M., Artaxo, P., Wagner, T., Pöschl, U., Andreae, M. O., and Pöhlker, C.: African volcanic emissions influencing atmospheric aerosols over the Amazon rain forest, Atmos. Chem. Phys., 18, 10391–10405, doi:10.5194/acp-18-10391-2018, 2018a.

Saturno, J., Holanda, B. A., Pöhlker, C., Ditas, F., Wang, Q. Q., Moran-Zuloaga, D., Brito, J., Carbone, S., Cheng, Y. F., Chi, X. G., Ditas, J., Hoffmann, T., de Angelis, I. H., Konemann, T., Lavric, J. V., Ma, N., Ming, J., Paulsen, H., Pöhlker, M. L., Rizzo, L. V., Schlag, P., Su, H., Walter, D., Wolff, S., Zhang, Y. X., Artaxo, P., Pöschl, U., and Andreae, M. O.: Black and brown carbon over central Amazonia: long-term aerosol measurements at the ATTO site, Atmos. Chem. Phys., 18, 12817–12843, doi:10.5194/acp-18-12817-2018, 2018b.

Su, H., Rose, D., Cheng, Y. F., Gunthe, S. S., Massling, A., Stock, M., Wiedensohler, A., Andreae, M. O., and Pöschl, U.: Hygroscopicity distribution concept for measurement data analysis and modeling of aerosol particle mixing state with regard to hygroscopic growth and CCN activation, Atmos. Chem. Phys., 10, 7489–7503, doi:10.5194/acp-10-7489-2010, 2010.

Su, L., and Fung, J. C. H.: Investigating the role of dust in ice nucleation within clouds and further effects on the regional weather system over East Asia – Part 1: model development and validation, Atmos. Chem. Phys., 18, 8707–8725, doi:10.5194/acp-18-8707-2018, 2018.

Tackett, J. L., Winker, D. M., Getzewich, B. J., Vaughan, M. A., Young, S. A., and Kar, J.: CALIPSO lidar level 3 aerosol profile product: version 3 algorithm design, Atmos. Meas. Tech., 11, 4129–4152, https://doi.org/10.5194/amt-11-4129-2018, 2018.

Tuccella, P., Curci, G., Visconti, G., Bessagnet, B., Menut, L., and Park, R. J.: Modeling of gas and aerosol with WRF/Chem over Europe: Evaluation and sensitivity study, J. Geophys. Res.-Atmos., 117, doi:10.1029/2011jd016302, 2012.

Wu, L., Su, H., and Jiang, J. H.: Regional simulations of deep convection and biomass burning over South America: 1. Model evaluations using multiple satellite data sets, J. Geophys. Res., 116, doi:10.1029/2011jd016105, 2011.

Zhang, Y., Zhang, X., Wang, K., He, J., Leung, L. R., Fan, J., and Nenes, A.: Incorporating an advanced aerosol activation parameterization into WRF-CAM5: Model evaluation and parameterization intercomparison, J. Geophys. Res.-Atmos., 120, 6952–6979, doi:10.1002/2014jd023051, 2015.

Zhuang, Y., Fu, R., Marengo, J. A., and Wang, H.: Seasonal variation of shallow-to-deep convection transition and its link to the environmental conditions over the Central Amazon, J. Geophys. Res., 122, 2649–2666, https://doi.org/10.1002/2016JD025993, 2017

Table S1. Monthly mean perturbations caused by the ARI effect of BB aerosols for the EMIS6 emission scenario.

	ARI in this study	PC3_EMISX - PCNR3_EMISX	difference
LWP (g m^{-2})	–3.8	–3.9	–0.1 (3%)
IWP (g m^{-2})	0.26	0.24	–0.02 (8%)

Table S2. Statistical indices of the comparisons between modeled and observed surface air temperature (T), relative humidity (RH), and wind speed (WS) at the ATTO site over September 2014.

	MB	RMSE	r
T (°C)	0.2	1.5	0.86
RH (%)	–2.3	9.2	0.78
WS ($m\ s^{-1}$)	–0.2	1.9	0.52

MB: the mean bias;
RMSE: the root mean square error;
r: the correlation coefficient.

Table S3. Comparison of AOD and SSA at 550 nm obtained from model simulation in domain3 and observation.

	Observation	Model[a]
	AOD	
Manaus_EMBRAPA (AERONET)	0.24±0.10 (average of Sep 2014)	0.21±0.05 (R[b]=0.54)
	SSA	
TT34[c] (Rizzo et al., 2013)	0.87±0.06 (average of Jul–Dec 2008–2010)	0.89±0.01
ATTO[d] (Saturno et al., 2018b)	0.88 (average of Aug–Nov 2012–2017)	0.90±0.01

a) Model results with EMIS1, averaged for September 2014.
b) R represents the correlation coefficient between the observation and model simulation.
c) The SSA values at this site are for 637 nm. Calculation of SSA at 550 nm is not conducted due to incomplete information on Angstrom exponent in Rizzo et al. (2013).
d) The SSA observation for the ATTO site is obtained from Saturno et al. (2018b) by extrapolating the original value at 637 nm to that at 550 nm using the Angstrom exponents in Saturno et al. (2018b).

Table S4. Estimates of radiative perturbation by biomass burning aerosols over the Amazon Basin in this study and from previous studies.

	Description	Radiative perturbation ($W\ m^{-2}$)*	AOD	Effect	Region of Amazon Basin	Model	Reference
Clear-sky	SW at TOA	–5.6±1.7	0.25±0.11	ARI	Southern	SBDART	Sena et al. (2013)
	SW at TOA	–3.33±0.89	0.48	total	Southern	HadGEM3-GA3	Thornhill et al. (2018)
	SW at TOA	[–0.7, –3.7]	0.2–0.6	ARI	Central	WRF-Chem	This study
All-sky	SW at TOA	1.35±1.8	0.48	total	Southern	HadGEM3-GA3	Thornhill et al. (2018)
	LW at TOA	–3.07±1.55					
	SW at surface	–5.46±1.93					
	SW at TOA	–1.75	0.8–1.2	ARI	Southwest	WRF-Chem	Archer-Nicholls et al. (2016)
		2.72	0.4–1.0				
		1.53	0.4–1.0				
	SW+LW at TOA	–4±1		ARI	Southern	MetUM	Kolusu et al. (2015)
	SW+LW at surface	–9±1					
	LW at TOA	–0.12		total	entire	WRF-Chem	Wu et al. (2011)
	SW at surface	–15.9					
	SW at surface	–28.23	0.633	total	Southern	GATOR-GCMOM	Ten Hoeve et al. (2012)
	LW at surface	8.6					
	SW at surface	–10	0.2–0.4	ARI	Southern	CCATT-BRAMS	Rosario et al. (2013)
	SW at TOA	[–0.3, 0.6]	0.2–0.6	total	Central	WRF-Chem	This study
	LW at TOA	[0.1, 0.9]					
	SW at surface	[–6.3, –31.8]					
	LW at surface	[0.3, 1.9]					
	SW at TOA	[0.4, 2.0]	0.2–0.6	ARI	Central	WRF-Chem	This study
	LW at TOA	[0.1, 1.0]					
	SW at surface	[–5.7, –30.5]					
	LW at surface	[0.3, 2.0]					

*Radiative perturbation with standard deviation or in bracket for range obtained from simulations with emission intensity of EMIS1–EMIS6.

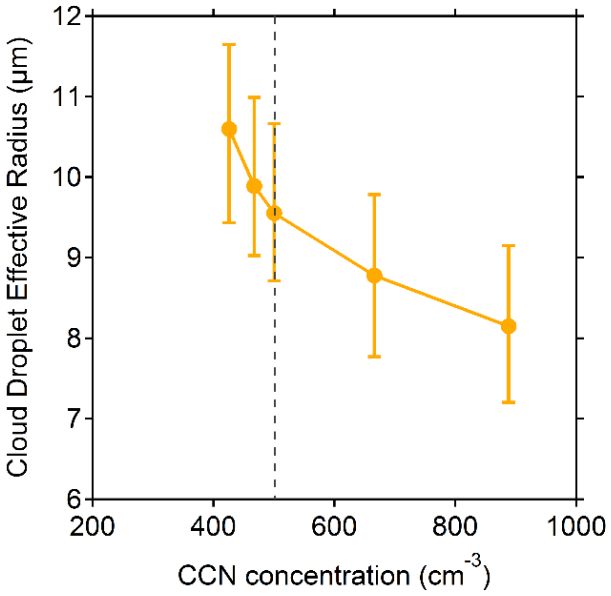

Figure S1. Relationship of monthly mean domain-averaged cloud droplet effective radius and cloud-base CCN concentrations for all emission scenarios derived from experiments of CCNR3 and PCNR3_EMISX. The dashed line indicates the EMIS1 scenario. Error bars represent the 25th and 75th percentiles of all domain-averaged data in each simulation.

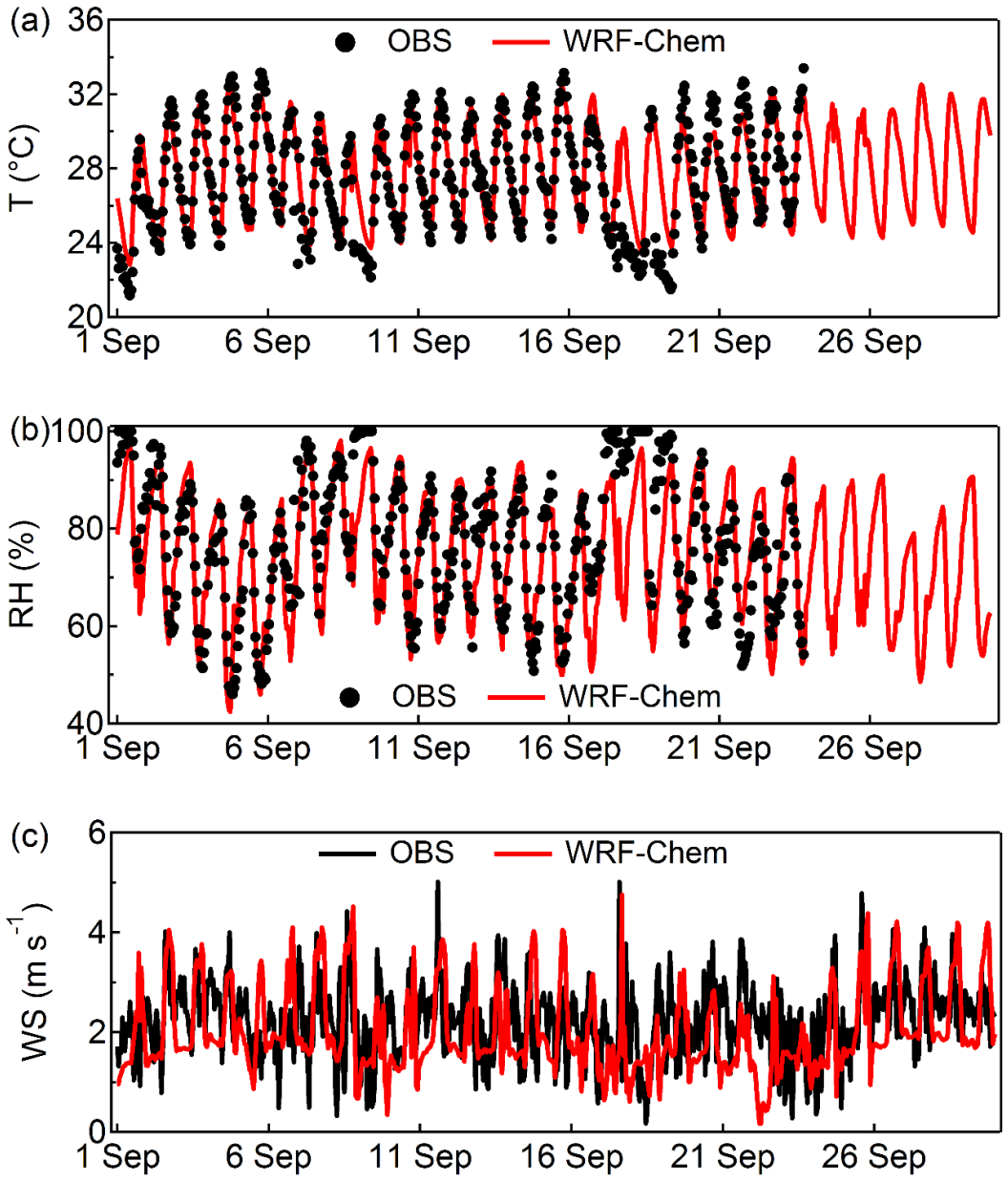

Figure S2. Time series of (a) surface air temperature, (b) relative humidity, and (c) wind speed from the domain3 simulation and the observations at ATTO during September 2014.

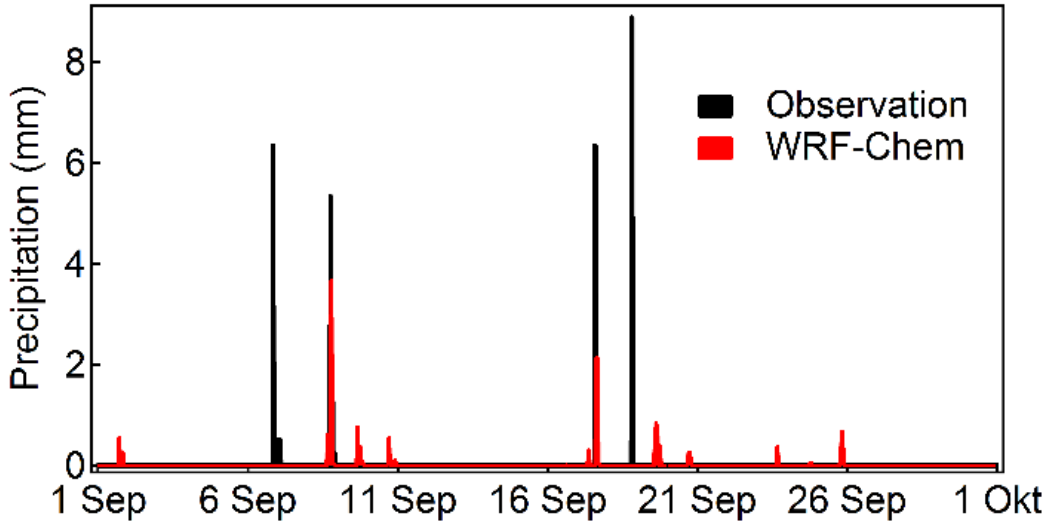

Figure S3. Time series of precipitation from observations at the ATTO site and WRF-Chem simulations during September 2014.

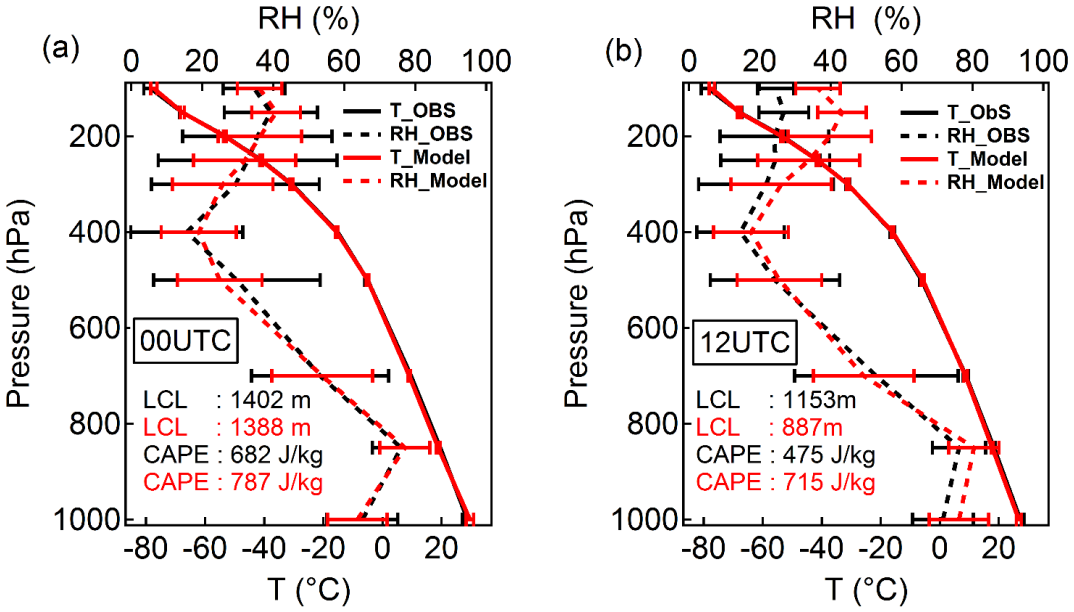

Figure S4. Vertical profiles of air temperature and relative humidity at standard levels, and retrieved CAPE and LCL values from radiosonde observations and WRF-Chem domain3 simulations at (a) 00:00 UTC and (b) 12:00 UTC at Manaus. Error bars at each pressure level represent the standard error at that level.

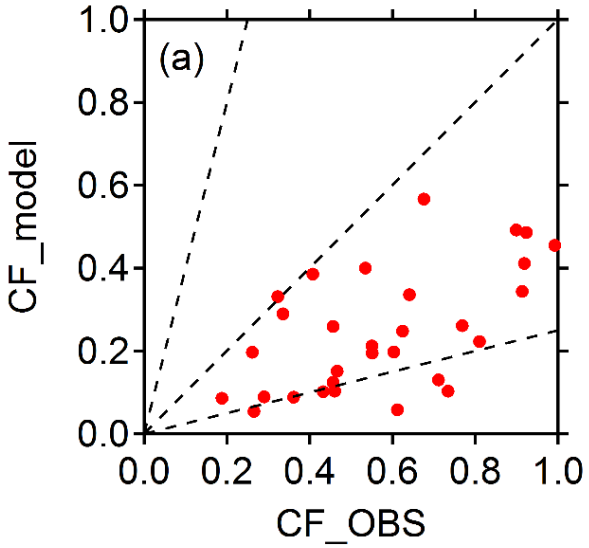

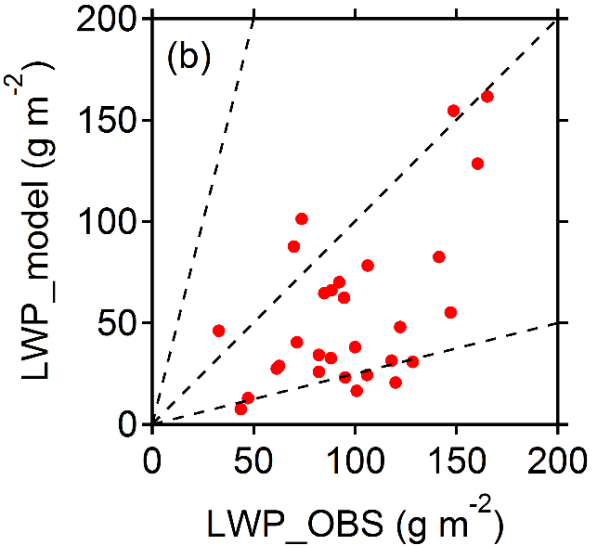

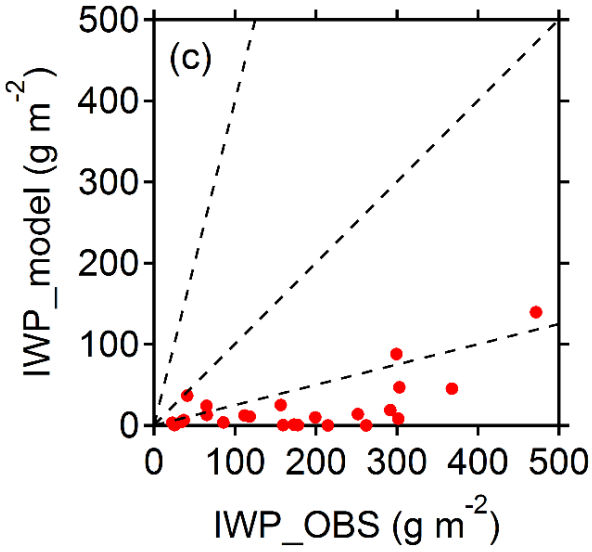

Figure S5. Scatter plots of (a) cloud fraction, (b) total liquid water path, and (c) total ice water path from WRF-Chem domain3 simulations and MODIS satellite measurements. The dashed lines are 1:4, 1:1, 4:1 from top to bottom, respectively.

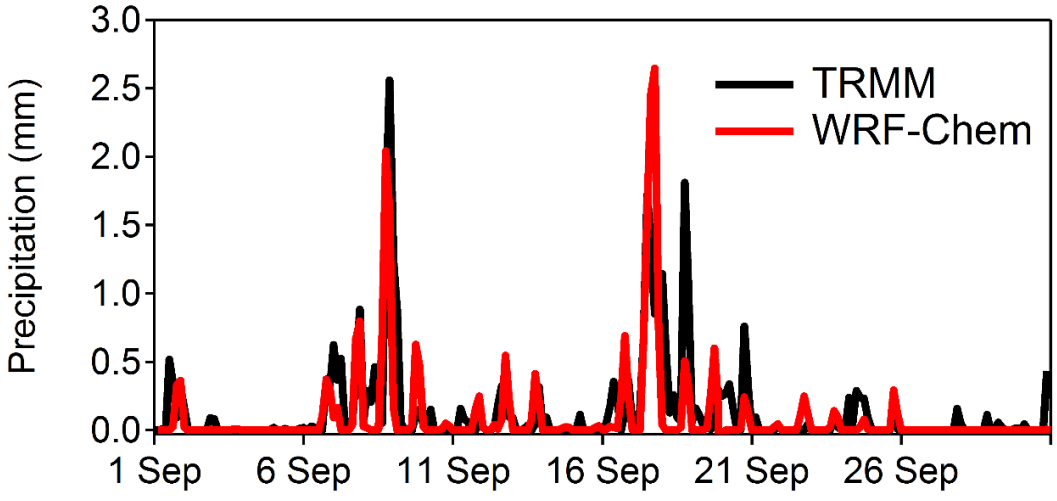

Figure S6. Time series of region averaged 3-hour accumulated precipitation (mm) over domain3 from TRMM satellite observations and WRF-Chem simulations during September 2014.

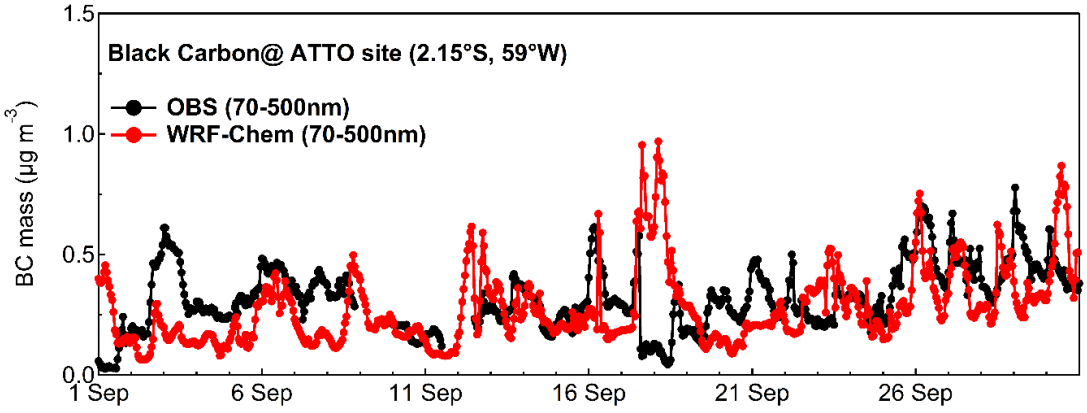

Figure S7. Time series of simulated and observed black carbon mass concentrations at the ATTO site.

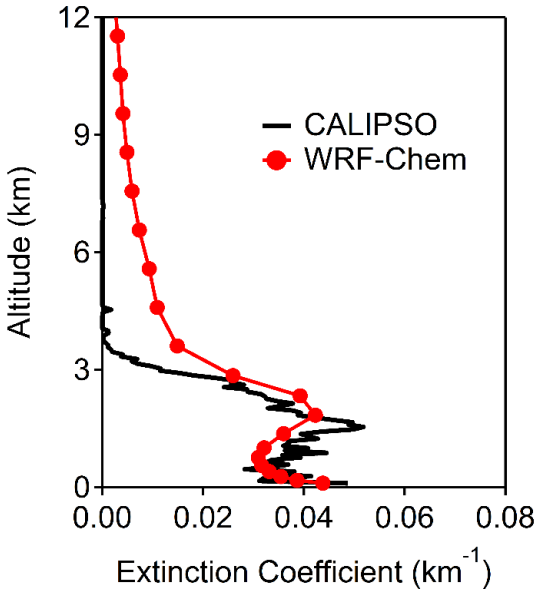

Figure S8. Monthly mean clear-sky aerosol extinction coefficient at 532 nm averaged over domain3.

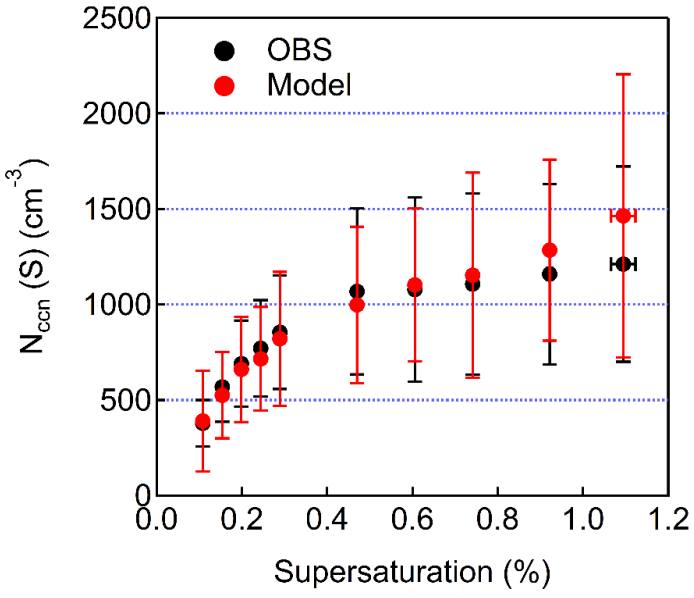

Figure S9. Monthly averaged CCN number concentrations at different supersaturations from ATTO observations and WRF-Chem simulations. Error bars represent the standard deviation.

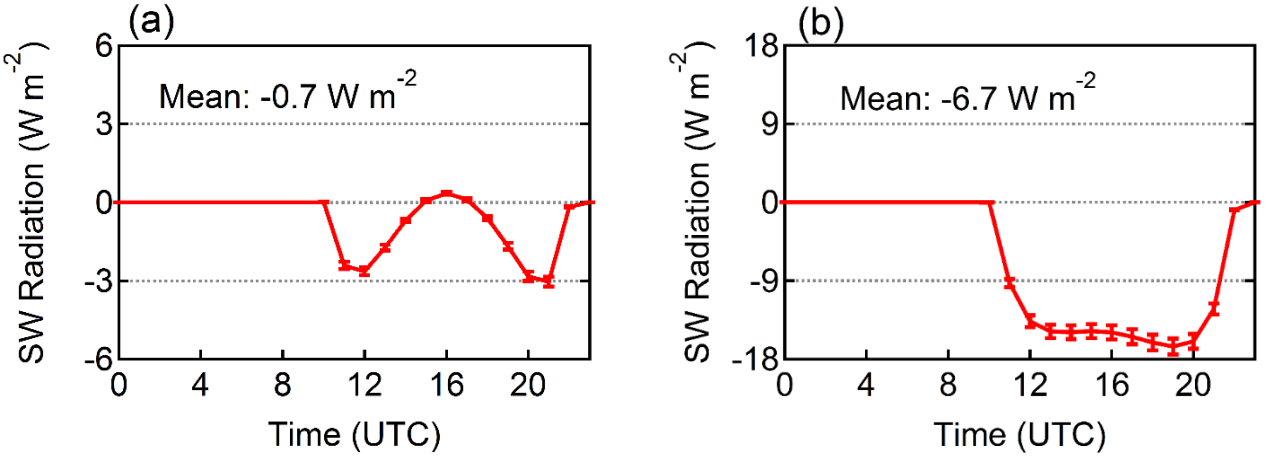

Figure S10. Diurnal variation of changes in clear-sky shortwave radiation at (a) TOA and (b) surface due to ARI in the EMIS1 emission scenario. Error bars denote the standard error.

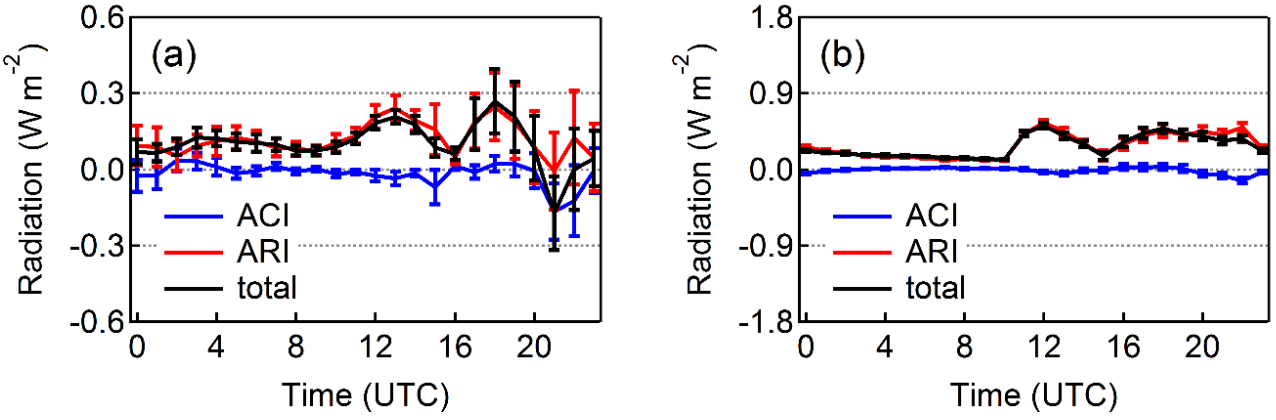

Figure S11. Diurnal variation of changes in all-sky longwave radiation at (a) TOA and (b) surface in the EMIS1 emission scenario. Error bars denote the standard error.

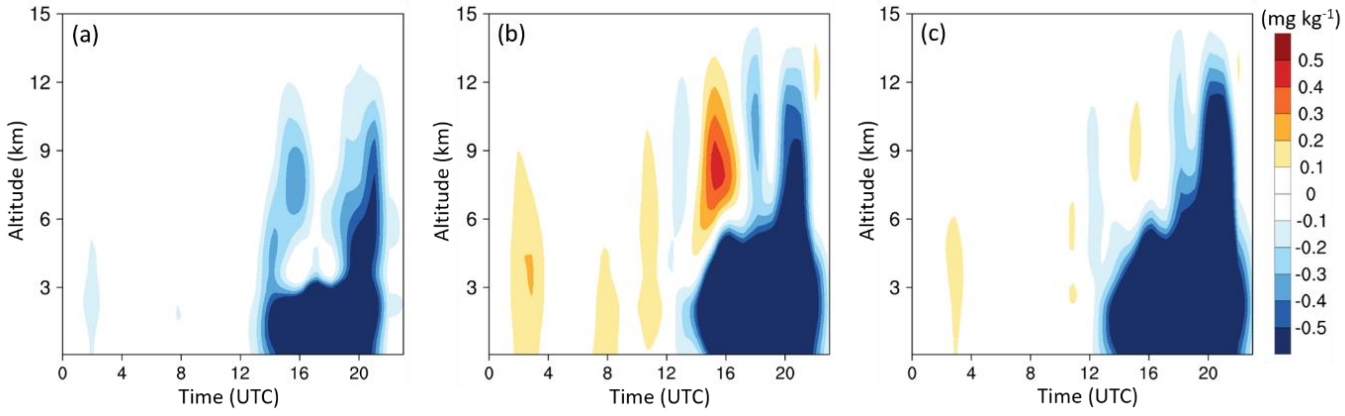

Figure S12. Diurnal variation of the vertical distribution of the domain-averaged difference in precipitating hydrometer (QRAIN+QSNOW+QGRAUP) concentrations caused by BB aerosols' (a) ACI, (b) ARI, and (c) total effect in the EMIS6 emission scenario.

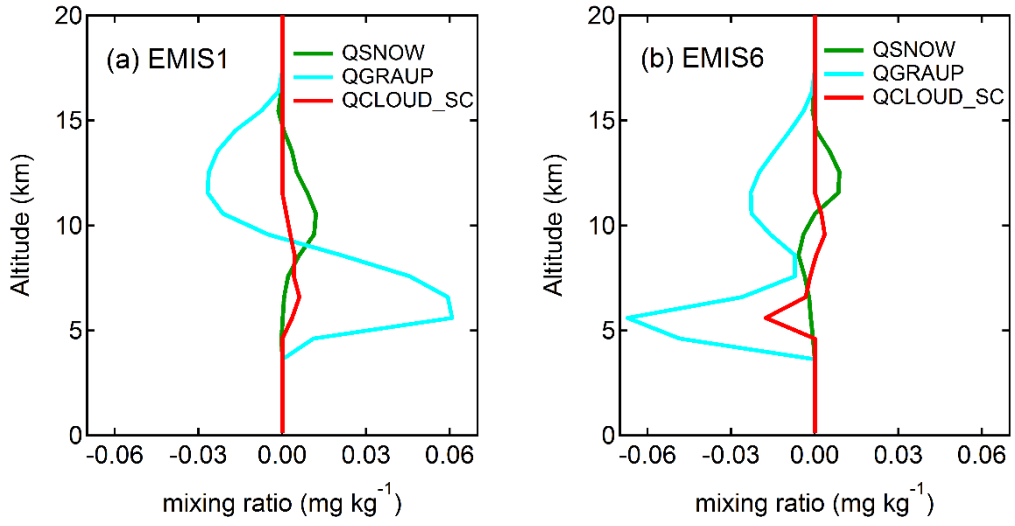

Figure S13. Profiles of ARI-induced changes in snow, graupel, and super-cooled cloud water mixing ratios for emission scenarios (a) EMIS1 and (b) EMIS6.

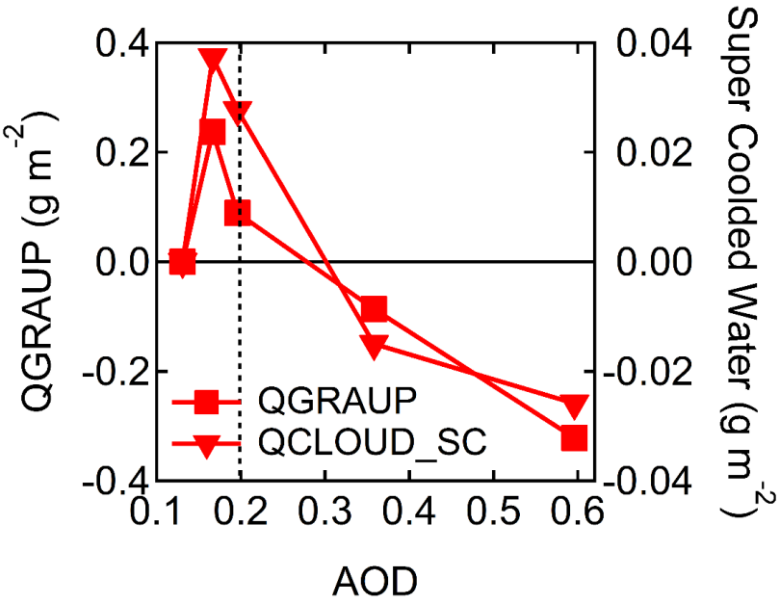

Figure S14. ARI-induced changes in column-integrated graupel and super-cooled cloud water content with increasing BB emission intensity (indicated by the domain-averaged AOD in each emission scenario). The vertical dotted line indicates the EMIS1 scenario.